

Arrayed silicon-based concave microlens fabricated by single mask ultraviolet-photolithography and dual-step KOH etching

Bo Zhang^{a,b}, Taige Liu^{a,b}, Zhe Wang^{a,b}, Wenhai Huang^{a,b}, Chai Hu^{a,b,c},
Kewei Liu^{a,b}, Mingle Chen^{a,b}, Jiashuo Shi^{a,b} and Xinyu Zhang^{a,b,*}

^aHuazhong University of Science and Technology, National Key Laboratory of Science and Technology on Multispectral Information Processing, Wuhan, China

^bHuazhong University of Science and Technology, School of Artificial Intelligence and Automation, Wuhan, China

^cHuazhong University of Science and Technology, Innovation Institute, Wuhan, China

Abstract

Background: As an important optical element, concave microlens arrays are utilized in many applications. How to fabricate a mass of concave microlens arrays efficiently at a low cost is a key problem to be solved.

Aim: We propose a method of fabricating a concave microlens array based on single mask ultraviolet (UV)-photolithography and dual-step potassium hydroxide (KOH) etching, which has proven to be efficient.

Approach: An arrayed silicon-based concave microlens utilized in the infrared wavelength range was designed and fabricated based on single mask UV-photolithography and dual-step KOH etching. Combining the computation simulation and the evolving microstructural mechanism based on the silicon anisotropic corrosion characteristics in a common KOH solution with several control factors such as the solution concentration, temperature, and corrosion period, an arrayed concave microlens with a spherical profile over a silicon wafer with the required crystal orientation was simulated, designed, and fabricated effectively.

Results: Both the scanning electron microscopy and the surface profile measurements indicate that the fabricated concave microlens arrays present a high filling-factor of more than 80% and a small surface roughness with a root mean square value in several tens of nanometer scale. The common optical measurements demonstrate that the fabricated silicon-based concave microlens presents a good infrared beam divergence performance.

Conclusions: The method highlights the prospect of the industrial production of large-area silicon-based concave microlens arrays for infrared beam shaping and control light applications.

© The Authors. Published by SPIE under a Creative Commons Attribution 4.0 International License. Distribution or reproduction of this work in whole or in part requires full attribution of the original publication, including its DOI. [DOI: [10.1117/1.JOM.2.2.023501](https://doi.org/10.1117/1.JOM.2.2.023501)]

Keywords: microlens array; MEMS; silicon wet etching.

Paper 21025G received Dec. 11, 2021; accepted for publication Mar. 10, 2022; published online Apr. 7, 2022.

1 Introduction

Concave microlens arrays fabricated over typical quartz or silicon wafer demonstrate an important ability of uniformly diverging incident beams in the visible or infrared wavelength range, which are already utilized in many applications such as optical scanners,¹ diffusers,² digital display units,³ biomedical instrumentation,⁴ optical communications,⁵ and other microelectromechanical systems (MEMS).^{6,7} Silicon concave microlens has been successfully used as a mold for a continuously electroplating metal mold or directly replicating plastic microlens.^{8,9}

*Address all correspondence to Xinyu Zhang, x_yzhang@hust.edu.cn

As shown, many fabrication methods have been developed for effectively shaping concave microlens with the required appearance according to a refract or reflect lightwave strategy, for example, common ultraviolet (UV)-photolithography combining melting, wet potassium hydroxide (KOH) etching,¹⁰ ion beam etching,^{11–13} impressing or embossing,^{14,15} microdroplet jetting,¹⁶ ultraprecise machining process such as typical diamond cutting or grinding,^{17,18} three-dimensional (3D) printing or imprinting,^{19–22} thermal reflowing,^{23,24} laser,^{25–27} electron beam direct writing or electrochemical method,²⁸ and so on. Generally, the methods mentioned above all present some intrinsic disadvantages. Common UV-photolithography and laser direct writing are unsuitable for fabricating microstructures with a complex contour or relief appearance based on finely defining exposure doses. The low-cost impressing or embossing manipulation highly relies on the interface coupling properties between the processed materials and the patterned mold with a featured nanometer size. With current microdroplet jetting, it is usually hard to control the consistency and microstructural size of each pixel micro-nano-domain shaped by overlapping jetting droplets for the fitting surface profile leading to the designed appearance of microlens.²⁹ As demonstrated, many refractive or diffractive microlens can be acquired by ultraprecise machining, which presents a tedious and expensive feature that creates a bottleneck for fabricating microdevices with relatively large sizes. At present, large-scale lens arrays can be fabricated by laser direct writing technology based on gray exposure and high-speed 3D printing technology. The imprinted profile of the microstructures cannot be completely the same as that of the mold because of the residual surface stress or microstructural mismatching between the mold and the optical materials processed. The contact angle between the arc boundary of a single microlens and the connected facets of the substrate is only determined by the wettability of the thermal reflow material over the substrate used and their surface tension, so it is very difficult to shape microstructure with a required or even arbitrary profile using nano-imprint technology.²⁹ The expensive electron beam direct writing is obviously not suitable for mass production of microlens.

We propose an efficient method for designing and fabricating spherical concave microlens based on single mask UV-photolithography and dual-step KOH etching of silicon wafer. The first-step KOH etching is carried out to form the initial inverted pyramid microholes with the required size over the silicon wafer, and the second-step KOH etching shapes the fitted profile with the desired surface roughness by connecting or even overlapping adjacent spherical silicon microholes. At first, an arrayed initial square micro-opening with the required aperture and arrangement is designed for inductively performing wet KOH etching to acquire the spherical profile of the target concave microlens. The intermediate profile information is repeatedly input into the simulation program that has already adopted a mature iterative algorithm to optimally minimize the surface roughness, which is mainly determined by the small bump-shaped during edge connecting or overlapping of the adjacent arc subprofiles of the silicon microholes with a given appearance. Thus, a photomask layout is patterned according to the aperture data and the location coordinate of each micro-opening exported from the computer program. Next, the photomask pattern is transferred onto the silicon wafer by single common UV-photolithography. Finally, an arrayed concave microlens over silicon wafer is made by dual-step KOH etching according to suitable technological conditions, thus demonstrating the low-cost and high-efficiency features attributed to the basic silicon anisotropic corrosion in the common KOH solution, which is compatible with current standard microelectronic technologies. The method highlights a way to manufacture large-area concave microlens arrays for infrared beam shaping and imaging applications at a low cost.

As shown, the key to adaptively designing the concave profile of a single microlens according to the algorithm through an optimal fitting subprofile of each silicon microhole with different geometric dimensions is to correctly select the size of the initial square micro-openings and then rational map them. The proposed method demonstrates great flexibility and designability for shaping a relatively complex surface profile of concave microlens. Moreover, the fabricated silicon microstructures can also serve as a mold to continuously perform typical embossing or impressing. According to the method proposed, a set of concave microlens arrays of 512×512 with a relatively high filling-factor of more than 80% and different concave depths from a typical value of ~ 1.0 to $2.0 \mu\text{m}$ have been successfully fabricated over silicon wafers.

Common measurements present a very low root mean square (RMS) surface roughness in several tens of nanometer scale and an ideal control infrared beam performance.

2 Designing Surface Profile of Silicon Concave Microlens

As demonstrated, the chemical corrosion of the silicon microstructures in a common KOH solution is anisotropic.¹¹ This property can be utilized to shape the initial inverted pyramid with different microstructural sizes resulting from a rapid first-step KOH etching of the {100} oriented silicon facet, which will be further evolved into a spherical microhole during another isolated second-step KOH etching.³⁰ In general, the geometry, such as the aperture and the depth of a single silicon microhole, can be easily changed by adjusting the side length of the square facet. The aperture of the final silicon microhole will be enlarged obviously, but the depth is almost kept invariant as only prolonging the KOH corrosion period corresponding to an initial inverted pyramid with a defined appearance corresponding to the micro-opening is performed in silicon dioxide (SiO₂) film. By carefully arranging a large number of initial square micro-openings and then configuring the window aperture for exposing each {100} oriented silicon facet to the KOH solution, a similar spherical profile can be fitted by connecting or even overlapping adjacent silicon microholes and thus finally be fixed after finishing the wet KOH corrosion. Thus, the layout composed of a large number of micro-openings corresponding to a spherical surface over {100} oriented silicon wafer can be designed through performing a microprofile fitting computation based on a quantitative expression of the anisotropic corrosion characteristics of the silicon microstructures in the KOH solution. Thus, a greedy algorithm is adopted to construct the final profile with featured surface roughness.

Figure 1 shows a typical course of shaping a single concave microlens with a circular aperture and a concave surface over {100} oriented silicon wafer by fitting several subprofiles of silicon microholes with different geometrical sizes. The top view of an ideal single silicon microlens with a concave depth of 2.0 μm is shown in Fig. 1(a). A relatively large circle with a radius of 224 μm as a target profile is orderly fitted by several small circular profiles, as shown in Fig. 1(b). According to the featured data of the target profile, the local deepest position A can be found while the target profile is traversed by the proposed greedy algorithm, as shown in Fig. 2(c). Thus, a concave spherical profile for fitting a fractional target profile around points A within the smallest tolerance or error should be as large as possible. As shown in Fig. 1(d), the fractional target profile between points B1 and B2 has been fitted well using a concave spherical profile with a radius of R_1 . But the fitted error does not meet the requirement of the sections from points B1 to T1 and from points B2 to T2. Considering the case that points B1 and B2 are already the deepest positions in two sections, two concave spherical profiles with a radius of R_2 and R_3 should be added to carefully fit the target fractional profile around points B1 and B2. Thus, two other concave spherical profiles are obtained, and then the positions and radius R_2 and R_3 are recorded. Both sections from points C1 to T1 and from points C2 to T2 should be further fitted because the errors are still relatively large. As shown in Fig. 1(e), two other concave spherical profiles are obtained, and thus the position and the radius R_4 and R_5 are recorded according to the proposed method. The sections of the target profile from points D1 to T1 and from points D2 to T2 can also be fitted continuously. According to the required initialization technological parameters and the concave sphere structural characters such as R_1, R_2, R_3 , and so on, the side lengths of the square micro-openings can be calculated as L_1, L_2, L_3 , and so on, and their positions can also be distributed at the center of each concave spherical pattern. After that, the key layout obtained from the algorithm about the arranged micro-openings leading to the required silicon concave profile for fully fitting the target profile is demonstrated in Fig. 1(f), where a red linear square micro-opening with a suitable aperture and indicated by dotted frames is also inserted. Usually, the largest silicon microhole is established at the center of the concave microlens, and the aperture of each microhole is then gradually decreased. Thus the center-to-center distance between adjacent microholes also lengthened along the radial direction, which means that the smallest microholes should be located at the edge corresponding to the constructed concave microlens. The fine patterns of the photomask are also formed according to the proposed layout.

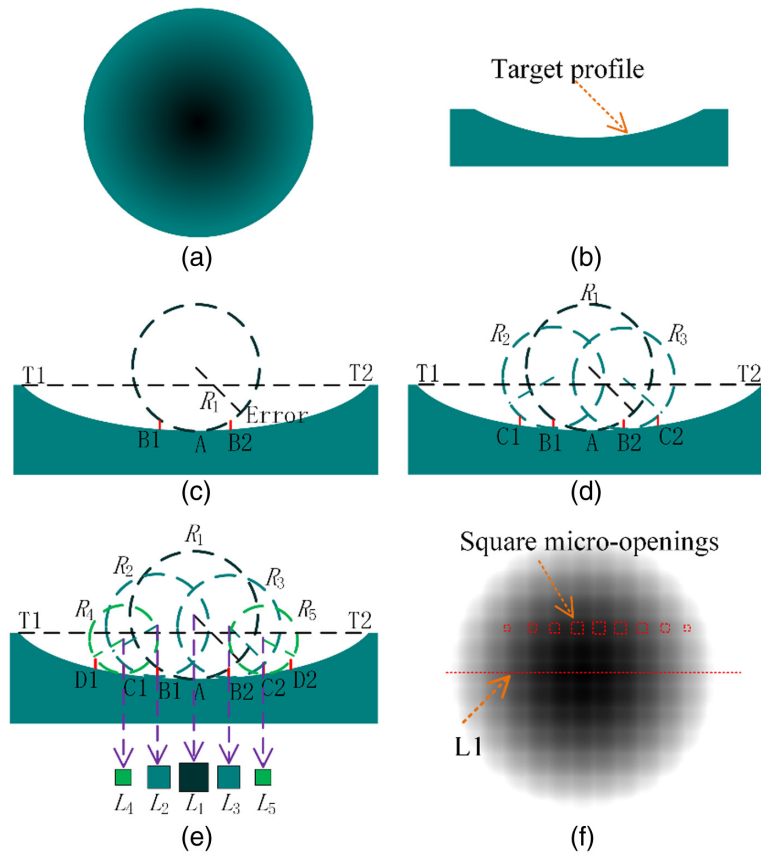


Fig. 1 Fitting of several subprofiles with different apertures and depths for shaping a single concave microlens. (a) Top view of a single concave microlens with the required size and appearance. (b) A cross-section of the target profile is expressed by a concave sphere with a curvature radius of $224\ \mu\text{m}$ and a concave depth of $2\ \mu\text{m}$. (c) The first step of the greedy algorithm and the fractional target profile from points B1 to B2 fitted by an arc with a radius of R_1 . (d) The second step of the greedy algorithm and the fractional target profiles from points B1 to C1 and from points B2 to C2 fitted by two arcs with different radii of R_2 and R_3 , respectively. (e) The second step of the greedy algorithm and the fractional target profiles from points C1 to D1 and from points C2 to D2 fitted by different arcs with a radius of R_4 and R_5 , respectively. (f) Top view of the surface morphology fitted by several microholes with different depths and a similar aperture, a partial layout of linear micro-openings corresponding to the microholes is inserted over the central axis.

During technological experiments, the patterned micro-openings with suitable aperture and size are firstly defined into a 200-nm thick SiO_2 film precoated over a $\{100\}$ oriented silicon wafer by single UV-photolithography and common inductively coupled plasma (ICP) etching. ICP etching is a dry etching technique widely used in the fabrication of micro-nano-devices. Then, the dual-step KOH etching is carried out to form the concave microlens. The typical fitting through connecting the edge of the adjacent microholes to form the final concave surface and the fitting error is shown in Fig. 2. Figure 2(a) is a cross-section diagram along line L1 in Fig. 1(d). As demonstrated in Fig. 2(a), several obvious bumps with different heights arise between adjacent subprofiles, causing the error between the fitted and the target profiles. Thus, the error character for surface roughness estimation should be analyzed carefully. Figure 2(b) demonstrates the detailed surface appearance and the edge contour corresponding to the microlens mentioned above. As shown, the fitted and target profiles are not overlapped completely, which can be expressed by both the surface roughness and the edge regularity. As demonstrated by the enlarged picture of Fig. 2(c), the difference between the fitted and the target profiles mainly comes from continuous KOH etching of each microhole preshaped over the surface of the silicon wafer, which usually originates from several obvious bumps generated between adjacent subprofiles, as indicated by Fig. 2(d). These decide the surface roughness and the contour regularity

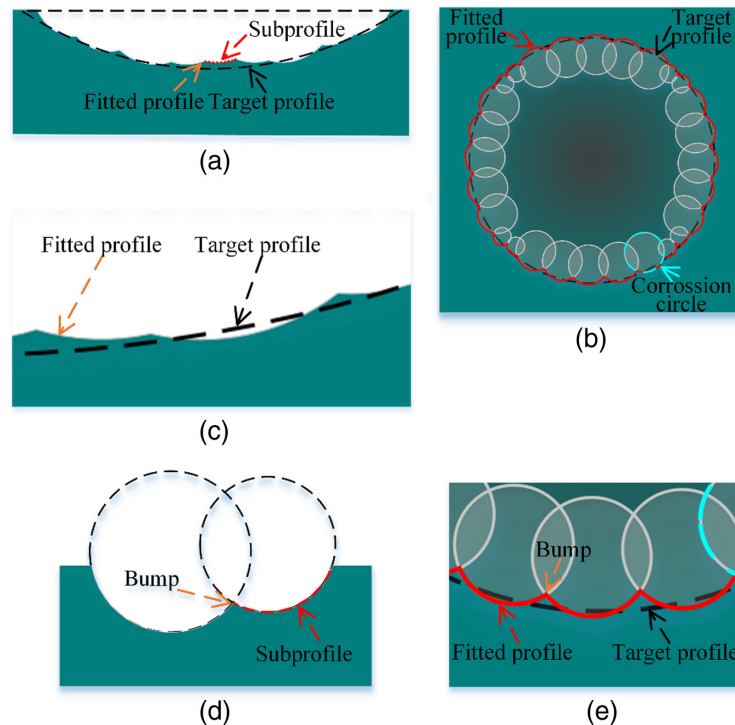


Fig. 2 Surface profile fitting and the featured errors shaped by both the fitted and target profiles. (a) A cross-section of the fitted and expected profiles of a concave microlens. (b) Top view of the fitted and expected edge contours of the microlens. (c) The partial enlarged fitting process leading to the target profile is indicated by a dotted line. (d) A surface bump error caused by intersecting two adjacent subprofiles with different sizes. (e) The zig-zag contour of the fitted edge targeted by an ideal smooth edge indicated by the dotted line.

of the final morphology of the silicon structures. The larger the size of the bumps is, the larger the RMS error is, and the worse the fitted profile fits the expected profile, so the microlens array function of focusing worsens. It should be noted that the surface profile of the microholes shaped by performing common wet KOH etching is already approximately expressed by a microcircle or a microsphere to conveniently predict the evolvement of the surface profile, which is another cause of surface errors. Thus, the final surface profile should be corrected empirically. Generally, both the height of the bumps and the depth of each valley under the dotted line, as shown in Fig. 2(c), can be further regulated to obtain the required RMS value.

As demonstrated in simulation computations, a surface roughness of ~ 27 nm corresponding to the target concave microlens with a curvature radius of ~ 224 μm and a depth of ~ 2 μm can be reached according to a set of initial parameters such as the KOH solution concentration of 30% at the working temperature of 60°C . Considering the situation that the fitted edge is not an ideal circle, as indicated by a red line in Fig. 2(e), an enlarged picture is exhibited to clearly present the edge intersection between fitted adjacent subprofiles, which demonstrates a zig-zag contour with very small errors. Because the RMS error between the fitted and target profiles of the concave microlens above is relatively small, the aperture and the location data of the square micro-openings generated from the computation simulation can be exported for subsequent photo etching and wet chemical corrosion processing. The initial micro-opening data created by the proposed algorithm are exported in common intermediate format (CIF) format and displayed based on a visual function provided by the simulation system.

The photomask layout for fabricating an arrayed concave microlens with a spherical appearance over a silicon wafer is shown in Fig. 3. To a single concave microlens, the detailed arrangement of the micro-openings with the required size for continuously shaping corresponding micro-openings in positive photoresist through single mask UV-photolithography and micro-opening-windows over the surface of the silicon wafer for undergoing a relatively strong wet KOH etching is shown in Fig. 3(a). As the final corrosion depth of the silicon microlens is

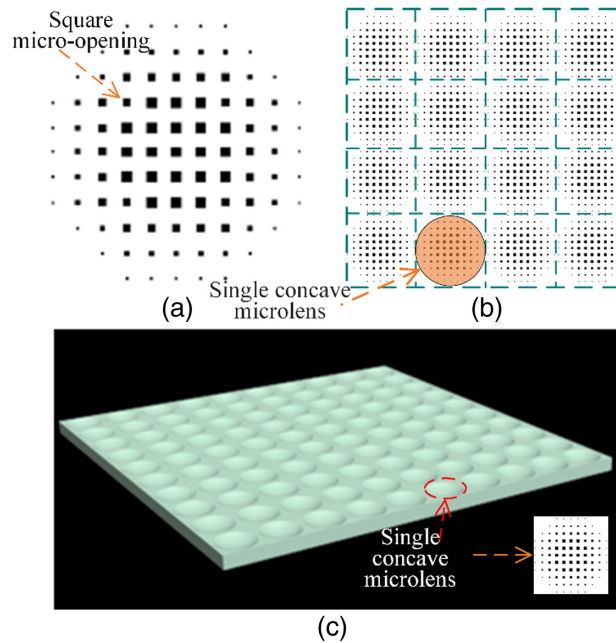


Fig. 3 Typical arrangement of the photomask for shaping an arrayed concave microlens. (a) Top view of a basic pattern in the photomask leading to a single concave microlens, where the black squares are micro-openings with different apertures. (b) Top view of the partial photomask for shaping an arrayed concave microlens. (c) Displaying the final concave microlens array.

decided by the large micro-opening, the micro-openings with the largest side length are arranged in the middle, and they maintain a relatively large center-to-center distance, thus with a small structural size distributed on the edge region in the photomask. The partial photomask for fabricating the silicon concave microlens array is shown in Fig. 3(b), where each dotted square frame corresponds to a single microlens as indicated by a circular shadow. A partial 3D display of the target concave microlens array is demonstrated in Fig. 3(c).

Combining the necessary technological parameters, a whole design leading to an arrayed silicon concave microlens with a depth of $2.0 \mu\text{m}$ is completed, and then the arrayed concave microlens with a concave depth of 1.0 , 1.2 , 1.4 , 1.6 , and $1.8 \mu\text{m}$, are further simulated, respectively, under the condition of the KOH solution concentration being $\sim 30\%$ at a working temperature of $\sim 60^\circ\text{C}$. The maximum micro-opening and the corrosion period corresponding to each simulation are given in Table 1. The parameters exported from an ideal simulation system are only references for guiding the technological processes. As the concave depth is gradually increased, the side length of the maximum micro-opening, as well as the corrosion period, should be increased to fit the deeper profile efficiently.

Table 1 Parameters for shaping an arrayed concave microlens.

Concave deep (μm)	Maximum opening (μm)	Corrosion period (min)
1.0	3.18	15.2
1.2	3.53	16.5
1.4	3.77	17.0
1.6	4.60	17.9
1.8	5.16	18.8
2.0	5.44	21.0

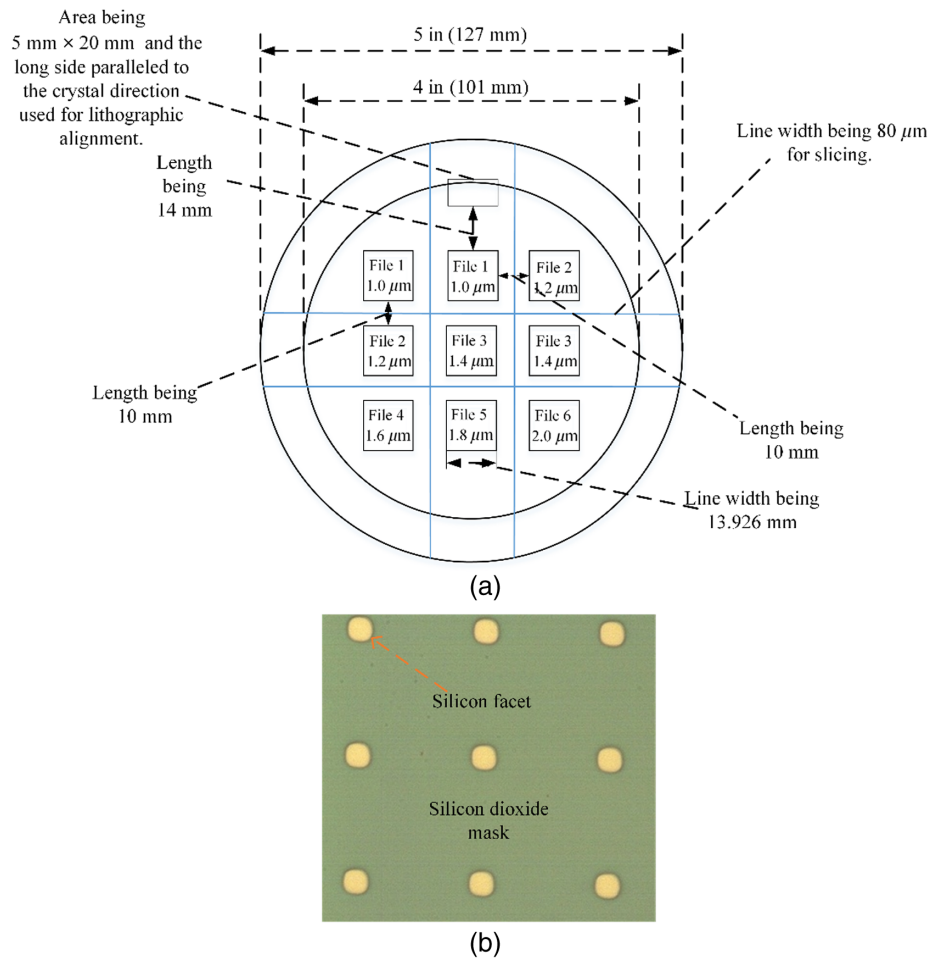


Fig. 4 Photomask of concave microlens arrays and local enlarged image of the concave microlens after ICP etching. (a) Photomask for fabricating the concave microlens arrays with different microstructural sizes. (b) Partial pale green SiO_2 mask patterned by shaping a large number of yellow silicon facets exposed for undergoing wet KOH etching.

3 Fabricating Concave Microlens Arrays

3.1 Single Mask Ultraviolet-Photolithography

The fabrication process includes two key procedures: single mask UV-photolithography and dual-step wet KOH etching. The detailed operations are as follows. The CIF data compiled according to the microstructural size of the concave microlens is exported from the simulation system, which is uniformly distributed in a circle with a 4-in diameter, as shown in Fig. 4(a).

Files 1 to 6 correspond to the arrayed concave microlens with a concave depth of 1.0, 1.2, 1.4, 1.6, 1.8, and 2 μm , respectively. To ensure the fabrication success rate corresponding to the microlens with a relatively small depth, two groups of microlenses with the same concave depth, including the value of 1.0, 1.2, and 1.4 μm , are made, as indicated in Fig. 4(a). The photomask is fabricated according to a standard square dimension of 5 in to match the photolithography apparatus. The horizontal and vertical distances between adjacent concave microlens arrays, each having a size of 13.926 mm \times 13.926 mm, are set as 10 μm , and the blue line width between adjacent microlens arrays is 80 μm for slicing. A small rectangle with an area of 5 mm \times 20 mm is configured at the top of the file region for lithographic alignment. Its long side is paralleled to the crystalline direction of the silicon wafer. At present, the patterned mask with an actual map error within $\pm 0.05 \mu\text{m}$ is made in chromium thin film at the Institute of Electrical Engineering, Chinese Academy of Sciences (Beijing, China).

Continuously, single mask UV-photolithography is carried out using a SUSS MA6/BA6 Double-sided UV Mask Aligner to thoroughly eliminate several obvious disadvantages in common technological processes such as a relatively large alignment error and a high fabrication cost during multiple-step photolithography to obtain similarly patterned microstructures as above. The key technological parameters include a SiO_2 protection film formation over the surface of the {100} oriented silicon wafer by traditional plasma-enhanced chemical vapor deposition of STS PECVD being ~ 200 nm, a deposition rate of more than 150 nm/min., uniformity, and the repeatability of $< \pm 5\%$.

Then, a SiO_2 mask composed of a large number of micro-openings with the same aperture and spatial arrangement as that in the photoresist film is shaped through dry ICP etching of STS Multiplex AOE. Finally, the residual photoresist materials attached over the surface of the SiO_2 mask are thoroughly removed to shape a pale green SiO_2 mask composed of a large number of yellow silicon facets exposed for undergoing subsequent wet KOH etching as shown in Fig. 4(b).

3.2 Dual-Step KOH Etching

As a typical chemical etching operation, the wet KOH erosion can be effectively used to shape fine microstructural patterns over the surface of the silicon wafer. Thus, the dual-step KOH etching process is adopted for shaping spherical concave microlens. The typical parameters are as follows: the KOH solution concentration is $\sim 30\%$, the working temperature is sustained at $\sim 60^\circ\text{C}$ using a constant temperature magnetic stirrer, and the KOH etching period is slightly longer to ensure that a complete corrosion process of the fine microstructures is performed. The common first-step etching period corresponding to those shown in Table 1 is ~ 10 min. The typical appearance of each inverted pyramid microhole processed by the first-step KOH etching is shown in Fig. 5.

As shown in Fig. 5(a), the local microscopic image of the fifth group in Table 1 demonstrates several identical inverted pyramid microstructures, where four side-facets of each inverted pyramid microhole are already divided by a shallow gray cross, as indicated in a grown array. The cross-section schematic is shown in Fig. 5(b). The inverted pyramid is formed by the first step KOH etching.

After completely removing the SiO_2 protection film, the silicon samples are put into the same KOH solution again to undergo the second-step KOH etching process. The corrosion period suitable to different silicon samples is in accordance with that shown in Table 1. It should be noted that the parameters shown in Table 1 only act as an indicator to guide the KOH etching processes. To ensure the fabricating accuracy, the silicon samples should be taken out from the reaction vessel to repeatedly observe their surface characters and microstructural details. The typical surface appearance evolving characters of the fifth group concave microlens array in Table 1 is shown in Fig. 6. As shown in Figs. 6(a) and 6(d), the microholes already reveal a relatively small bottom and aperture through KOH erosion of ~ 4 min. Meanwhile, the microhole is relatively shallow and small. The four small sidewalls of a single inverted pyramidal

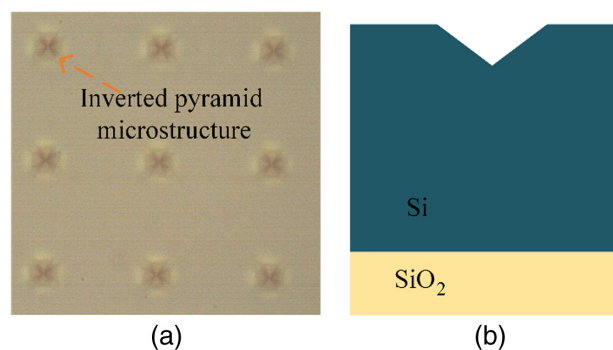


Fig. 5 The inverted pyramidal microstructures. (a) The inverted pyramidal microstructures formed over the surface of the silicon wafer after the first-step KOH etching. (b) The cross-section of the inverted pyramidal microstructures.

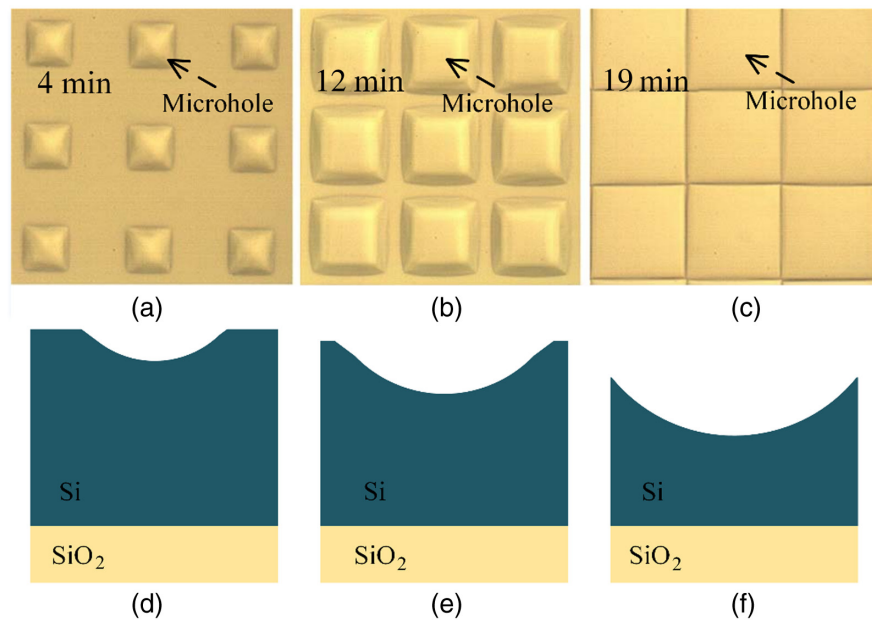


Fig. 6 The typical surface profile evolving characters of each microhole after undergoing different etching periods during a second-step KOH etching process and the etching process of the microhole. (a) Microholes with a relatively small aperture formed by the KOH erosion of ~ 4 min. (b) Extended microholes shaped by KOH etching of ~ 12 min, where four distinct residual sidewalls of each inverted pyramidal microstructure can still be viewed. (c) Ideal shallow microholes array with $\sim 100\%$ filling-factor after KOH etching of ~ 12 min. (d) The microhole is relatively shallow and small. (e) The microhole is getting larger and deeper. (f) The etching is nearly complete.

microstructure are still distinct. As shown in Fig. 6(b), extended microholes have been exhibited after ~ 12 min KOH etching, but their four residual sidewalls are still obvious. The microhole is getting larger and deeper, as shown in Fig. 6(e). As shown in Fig. 6(c), an ideal shallow concave microlens array with an $\sim 100\%$ filling-factor is finally shaped through KOH etching of ~ 19 min. The etching process is nearly finished and the microholes formed are shown in Fig. 6(f).

4 Measurement and Evaluation

4.1 Spherical Surface Appearance

The scanning electron microscope (SEM) photographs of the surface morphology of six groups of concave microlens arrays with different filling-factors including $\sim 80\%$, $\sim 90\%$, and $\sim 92\%$, corresponding to the focal length (f) of -37.77 , -31.55 , and -27.12 μm , respectively, are demonstrated in Fig. 7. In addition, the filling-factor of the other three lens arrays are $\sim 95\%$, $\sim 96\%$, $\sim 99\%$, respectively, and their respective focal lengths are -23.81 , -21.24 , and -19.20 μm . The maximum filling-factor of more than 99% is larger than that by the laser method, which is $\sim 96\%$ according to another paper.²⁷ As shown, the acquired silicon-based concave microlens arrays exhibit an identical microstructural appearance. For carefully comparing the microstructural characters, an enlarged facet of a single concave microlens attached by a simulation pattern with almost the same concave appearance but a slightly different edge profile is inserted in Fig. 7(a), which demonstrates the validity and reasonability of the proposed method. When analyzing the errors of the fitted and target profiles of the concave microlens, several microbumps caused by the KOH etching are seen in the enlarged picture; these can be further decreased by optimizing the simulation algorithm.

The concave depth and the structural uniformity of the fabricated silicon-based concave microlens are measured using step profiler KLA-Tencor P17, as demonstrated in Fig. 8. Figures 8(a) and 8(b) correspond to the first and third groups of the concave microlens arrays

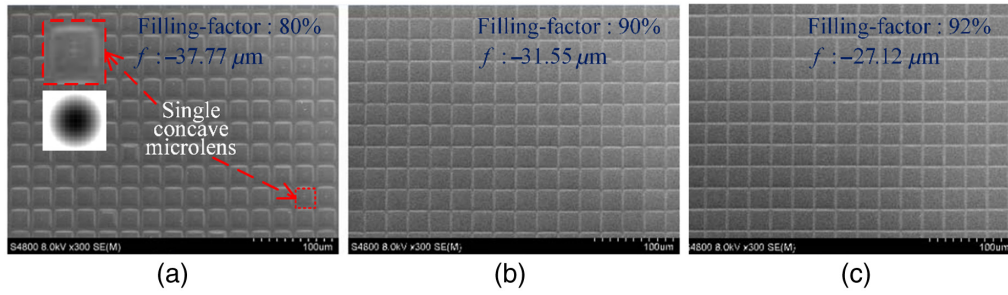
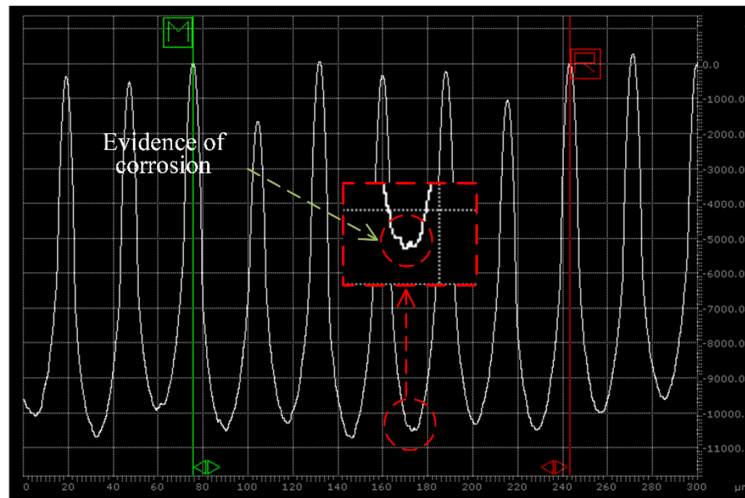
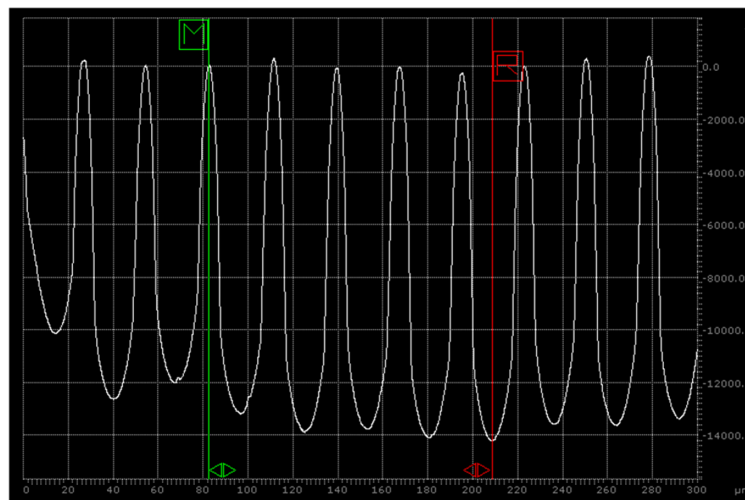


Fig. 7 SEM images of three groups of silicon-based concave microlens arrays fabricated according to the proposed method after dual-step KOH etching. Their key parameters (including concave depth, filling-factor, and focal length) of each concave microlens array are as follows: (a) ($\sim 1.0 \mu\text{m}$, $\sim 80\%$, $-37.77 \mu\text{m}$), (b) ($\sim 1.2 \mu\text{m}$, $\sim 90\%$, $-27.12 \mu\text{m}$), and (c) ($\sim 1.4 \mu\text{m}$, $\sim 92\%$, $-27.12 \mu\text{m}$).



(a)



(b)

Fig. 8 Measured surface profiles of the silicon-based concave microlens arrays. (a) A partial wavelike profile of the concave microlens with an average depth of $\sim 1.0 \mu\text{m}$ and inset of a red dotted square frame indicating a local microstructural fluctuation. (b) An arrayed concave microlens with an average depth of $\sim 1.4 \mu\text{m}$.

Table 2 Concave depth of the silicon-based concave microlens.

Designed value (μm)	Measured value (μm)	Error (nm)	RMS error (nm)
1.0	1.017	17	39
1.4	1.154	246	50
2.0	2.052	52	37

shown in Table 1, respectively. It should be noted that there exist some differences in both the concave depth and the structural uniformity of the concave microlens tested. By eliminating the factors such as the uneven placement of the silicon samples during measurement and the testing probe not moving along a suitable scanning path, the depth of every single concave microlens is basically the same, which indicates a fine microstructural uniformity.

As shown in Fig. 8(a), an enlarged fragment of the tested surface curve demonstrates a small fluctuation, indicated by a red square dotted frame, which is mainly caused by the overlapping of adjacent microholes during a KOH corrosion course of the microstructure shown in the top left in Fig. 7(a). The typical average depth and RMS error of the fabricated concave microlens demonstrated in Fig. 7 are further evaluated carefully, as shown in Table 2. According to the data, the error is the difference between the designed value and the measured value of the concave depth, the error being at 10 to 100 nm. The surface roughness can be expressed by the RMS error between the designed and measured values, which is already in a several tens of nanometer scale. Thus, the surface of the fabricated silicon-based concave microlens can be viewed as an optical mirror surface to satisfy the design requirement fully. However, the roughness of the microlens of Kendall et al.³⁰ is <5 nm, and its surface figure is within $0.5 \mu\text{m}$ of a perfect sphere. Due to the surface profile being fitted section by section of the concave spherical profile, the microbumps cannot be removed, so the RMS error is larger.

4.2 Optical Characteristics

The common optical properties of the silicon-based concave microlens arrays are acquired by common optical measurements. At first, the patterned surface of the silicon-based concave microlens is directly illuminated by a visible beam in the microscope, and then the reflective light fields are recorded, as shown in Fig. 9. By focusing the illuminating beams over the bottom of each concave microlens and any planar facet between adjacent concave microlenses, the common light reflection characters of the silicon sample can be viewed clearly and photographed. As shown in Fig. 9(a), there exists an arrayed small bright spot formed by reflective

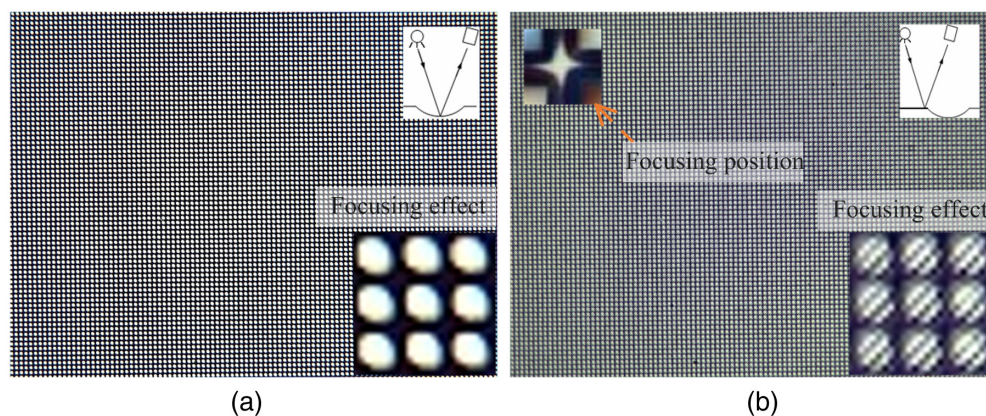


Fig. 9 Focusing illumination lightwaves of the microscope over different regions of an arrayed silicon-based concave microlens. (a) Focusing over the bottom of each concave microlens; the enlarged focusing effect is in the bottom right corner. (b) Focusing over the planar facets between adjacent concave microlenses; the enlarged focusing effect is in the bottom right corner.

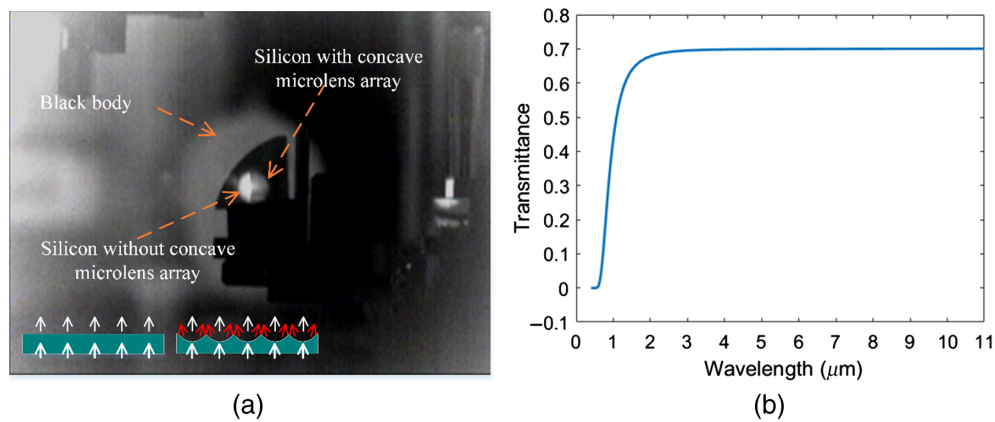


Fig. 10 The infrared testing of the microlens array. (a) Contrasting the infrared radiation distribution from a silicon wafer with a relatively large brightness at the left and from the silicon-based concave microlens with a dim shine. (b) A plot of the transmittance of the silicon sample without any microstructure in the wavelength range from 0.4 to 11 μm .

beams away from the smooth concave surface of each microlens that then constructs a uniform microcircular light spot distribution, which is captured by the objective of the complementary metal oxide semiconductor (CMOS) imager. As shown in Fig. 9(b), an arrayed quasi-cross-shaped light spot existing between four adjacent concave microlenses can also be viewed clearly; this is formed by the reflective beams focused at the planar facets between four concave microlenses, which then exhibit a uniform spatial distribution. The enlarged focusing effect at the bottom right corner is also different. The above measurements show that the silicon-based concave microlens array already meets the design requirements, indicating the effectiveness and feasibility of the proposed designing and fabricating method.

For evaluating the validity of the silicon samples further utilized in the infrared wavelength range, the fabricated silicon-based concave microlens arrays are then closely placed before the infrared radiation exiting window of the blackbody light source of Newport IR-564/301, which is set at $\sim 1000^\circ\text{C}$. The experimental allocation means that the silicon samples are directly illuminated by a beam of infrared lightwave from the blackbody. The penetrating light fields from the silicon samples are continuously captured by an infrared camera of Guide Infrared IR126. The key imaging measurement parameters are as follows: the waveband of ~ 8 to 12 μm , the focusing distance of ~ 40 mm, the F number of 1.2, and the field of viewing at $13.69^\circ \times 10.29^\circ$. Using a blackbody and an infrared camera, the divergence effect of the concave microlens array on infrared light can be observed intuitively.

A typical infrared image of the silicon sample and the plot of the transmittance of silicon are shown in Fig. 10. The infrared transmissivity of the silicon wafer is $\sim 60\%$ to 70% in Fig. 10(b), which is obtained by the finite-difference time-domain (FDTD) simulation. It can be seen that the output infrared light field can be obviously divided into two regions displaying different brightness levels in Fig. 10(a). One region corresponding to the silicon sample distributed by an arrayed concave microlens presents a relatively dim shine compared with another slightly smaller region of the silicon sample without any functioned microstructure. Generally, the infrared radiation can easily penetrate a thin silicon wafer, as demonstrated by a cluster of parallel arrows in the left inset of the figure. As indicated by small red arrows pointing to different directions in the right insert, a relatively strong beam divergence guided by the silicon-based concave microlens can be expected to result in an obvious decrease of the infrared radiation intensity measured along the main beam output direction from the infrared radiation exiting the window of the blackbody.

The detailed infrared beam divergence performance of the fabricated silicon-based concave microlens is further evaluated experimentally. The measurement principle and several main setups are shown in Fig. 11. The infrared beams from a selected aperture of the blackbody are directly incident upon the silicon sample, which are adhered onto an aluminum diaphragm of the blackbody utilized. Then, the infrared radiation penetrating the silicon samples is collected by a

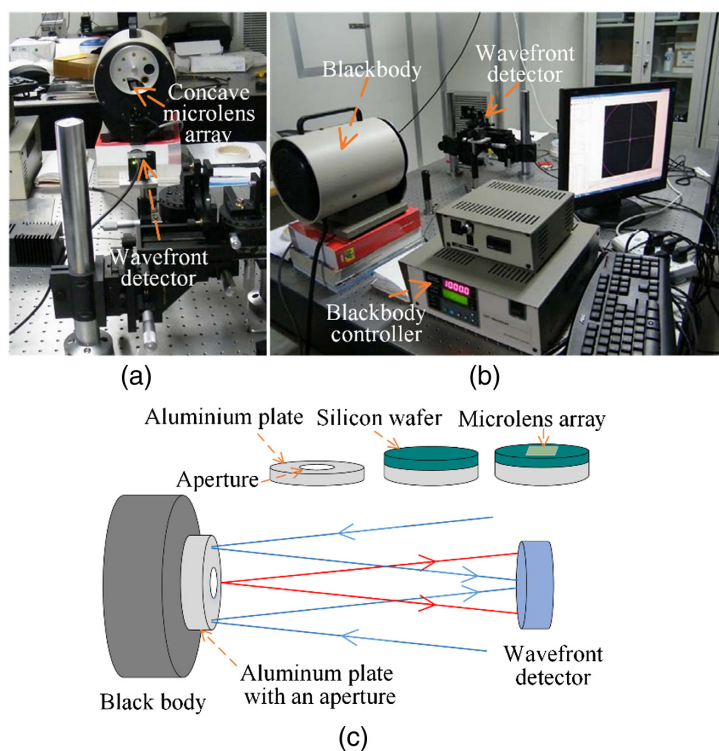


Fig. 11 Measurement principle and the main setup configuration. (a) The infrared radiation window of the blackbody and the silicon samples and the wavefront detector are aligned along the optical axis to form a measurement light path. (b) A typical case of performing wavefront test and construction. (c) Both the infrared target radiation and the environment light beams are received by the wavefront detector in an opening lab circumstance, where the red beams come from the blackbody and contain both the infrared and visible components and the blue represents the environment light in the visible range.

wavefront detector of Thorlab WFS150/WFS150C with a photosensitive range from ~ 200 to 1100 nm to obtain the infrared light field information from the silicon samples tested, as shown in Fig. 11(a). The distance between the silicon sample tested and the wavefront detector is ~ 47 cm, which should be carefully adjusted during experiments according to the size of the patterned region formed over the silicon samples. The typical case of the working temperature control of the blackbody and both the wavefront signal processing and display are shown in Fig. 11(b). The basic measuring optical path is given in Fig. 11(c). As indicated, the red infrared beams from the aperture of the blackbody are incident upon the silicon sample, and then the penetrating light fields already reshaped by the functioned microstructures formed over the measured silicon sample are captured by the wavefront detector. Because the measurements are carried out in an open lab environment, the blue environment lightwaves in the visible range are also captured by the wavefront detector.

The typical wavefront measurement results are shown in Fig. 12. As shown in Fig. 12, the top three pictures, indicated by Figs. 12(a)–(c), are spot diagrams, a measured curve along a straight line through the center of each concave microlens in the field of viewing of the wavefront detector, and a “composite wavefront,” which is acquired by measuring both the infrared radiation field and the circumstance light field in the visible range, respectively. As shown in Fig 12(b), both the top and bottom curves demonstrate a fairly uniform spatial distribution and almost the same signal amplitude according to the configurations of the convex refractive microlens array coupled with the sensor array in the wavefront detector, where the top curve corresponds to the blackbody radiation and the bottom to the environment light reflected from the thin aluminum supporter around the infrared radiation window of the blackbody into the wavefront detector. The pattern shown in the top of Fig. 12(c) can be roughly called a “composite wavefront” but not a real or actual light wavefront because the photoelectronic signal from the wavefront detector

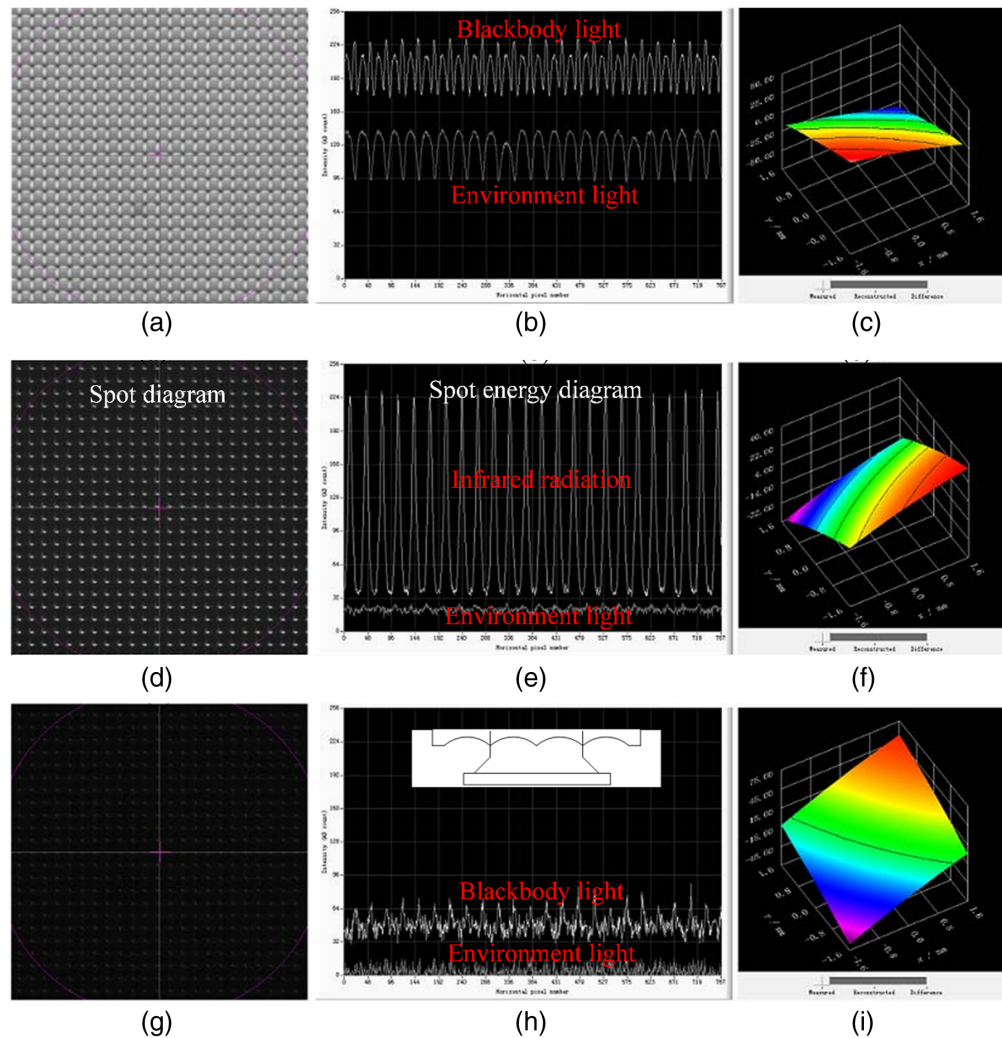


Fig. 12 Typical “composite wavefront” measuring results. (a) Spot diagram from the infrared radiation from the blackbody and the environment light field. (b) Spot energy diagrams of the blackbody radiation and the environment lightwaves reflected from the aluminum supporter. (c) A “complex wavefront” of the infrared radiation from the blackbody. (d) Spot diagram of the infrared radiation penetrating the silicon wafer without any concave microlens covering the radiation window of the blackbody. (e) Spot energy diagram of the infrared radiation from the silicon wafer without any concave microlens. (f) A “complex wavefront.” (g) Spot diagram of the infrared radiation going through an arrayed silicon-based concave microlens. (h) Corresponding spot energy diagram. (i) A corresponding “complex wavefront.”

for computing each sub-planar-wavefront incident upon each sub-sensitive-array in the total sensitive array is a sum of each photoelectronic spectral signal in a relatively wide wavelength range, with the top being in the visible and near-infrared range and the bottom being only in the visible range. From the flat morphology shown in Fig. 12(c), we know that the infrared radiation light field of the blackbody and the environment light field are fairly uniform. After covering a silicon wafer without a microlens array over the infrared radiation window of the blackbody, the typical measuring results are shown in Figs. 12(d)–(f), respectively. The two-dimensional (2D) spot diagram shown in Fig. 12(d) presents a uniformly converging light spot. As shown in Fig. 12(e), a linear infrared convergence curve has been remarkably amplified to almost threefold average amplitude compared with that shown in Fig. 12(b), considering the cases of the infrared transmissivity of the silicon wafer being $\sim 60\%$ and the environment light reflectance being very low.

The amplitude of the bottom visible light measuring curve is very low even though it is amplified with the same magnification as that of the top curve, but it presents almost one-third of the average amplitude compared with the bottom curve shown in Fig. 12(b). Thus, an inclined

planar “composite wavefront” due to the silicon wafer that is not parallel to the objective of the wavefront detector is acquired. After replacing the silicon wafer without any microlens with another silicon sample with an arrayed concave microlens arranged in its central region over the radiation window of the blackbody, the typical measuring results are shown in Figs. 12(g)–(i), respectively. A similar 2D light spot diagram with a relatively large brightness shown in Fig. 12(g) also presents a uniformly converging light spot. Figure 12(h) shows that an infrared radiation measuring curve with a weak wave-shaped fluctuation with a relatively low average amplitude is obtained. A very weak measuring curve of the environment lightwaves reflected from the aluminum supporter, which is similar to that of the bottom fluctuating curve shown in Fig. 12(e), can also be measured because the environment light field is unvaried during performing measurements. A similar inclined planar “composite wavefront” is also obtained. According to the experimental results, we know that an arrayed silicon-based concave microlens can be efficiently used to diverge incident infrared radiation to validate the effectiveness of the designing and fabricating method.

5 Conclusion

A practical method to quickly design, simulate, and fabricate an arrayed infrared concave microlens with a spherical profile, which is realized with single mask UV-photolithography and dual-step KOH etching, is proposed. The computation simulation is combined with the evolving microstructural mechanism based on the silicon anisotropic corrosion characteristics in a common KOH solution with several control factors, such as the solution concentration, temperature, and corrosion period, to make a concave microlens array over a silicon wafer with the required crystal orientation. Both the SEM and the surface profile measurements are carried out to obtain the key configurations, including the filling-factor of the concave microlens array and the surface roughness expressed by an RMS value. The filling-factor is ~99%. The RMS value in several tens of nanometer-scale meets the requirement of the optical mirror. In addition, all kinds of spherical or aspherical profiles can be designed and fabricated by this method. The common optical measurements demonstrate that the fabricated silicon concave microlens presents a good infrared radiation divergence character. The method highlights the prospect for industrial production of large-area silicon-based concave microlens arrays for infrared beam shaping and control light applications.

Acknowledgments

The authors would like to thank the editor and anonymous reviewers for their helpful comments.

References

1. G. Molar-Velazquez, F. J. Renero-Carrillo, and W. Calleja-Arriaga, “Two-dimensional optical micro-scanner on silicon technology,” *Optik* **121**(9), 843–846 (2010).
2. R. Bitterli et al., “Fabrication and characterization of linear diffusers based on concave microlens arrays,” *Opt. Express* **18**(13), 14251–14261 (2010).
3. F. Galeotti et al., “Microlens arrays for light extraction enhancement in organic light-emitting diodes: a facile approach,” *Org. Electron.* **14**(1), 212–218 (2013).
4. J. C. Roulet et al., “Fabrication of multilayer systems combining microfluidic and micro-optical elements for fluorescence detection,” *J. Microelectromech. Syst.* **10**(4), 482–491 (2001).
5. H. Toshiyoshi et al., “A surface micromachined optical scanner array using photoresist lenses fabricated by a thermal reflow process,” *J. Lightwave Technol.* **21**(7), 1700–1708 (2003).
6. M. Elwenspoek and H. V. Jansen, *Silicon Micromachining*, Cambridge University Press (2004).
7. P. Pal and K. Sato, *Silicon Wet Bulk Micromachining for MEMS*, Jenny Stanford Publishing (2017).

8. U. Köhler et al., "Fabrication of microlenses by plasmaless isotropic etching combined with plastic moulding," *Sens. Actuators A Phys.* **53**(1–3), 361–363 (1996).
9. J. Albero et al., "Fabrication of spherical microlenses by a combination of isotropic wet etching of silicon and molding techniques," *Opt. Express* **17**(8), 6283–6292 (2009).
10. D. W. D. L. Monteiro et al., "Single-mask microfabrication of aspherical optics," *Opt. Express* **11**(18), 2244–2252 (2003).
11. Y. Q. Fu and N. K. Bryan, "Semiconductor microlenses fabricated by one-step focused ion beam direct writing," *IEEE Trans. Semicond. Manuf.* **15**(2), 229–231 (2002).
12. Y. Q. Fu and N. K. A. Bryan, "Hybrid microdiffractive-microrefractive lens with a continuous relief fabricated by use of focused-ion-beam milling for single-mode fiber coupling," *Appl. Opt.* **40**(32), 5872–5876 (2001).
13. H. D. Kim et al., "Fabrication of a uniform microlens array over a large area using self-aligned diffuser lithography (SADL)," *J. Micromech. Microeng.* **22**(4), 2303–2309 (2012).
14. S. S. Deshmukh and A. Goswami, "Recent developments in hot embossing - a review," *Mater. Manuf. Process.* **36**, 1–43 (2020).
15. X. H. Lee et al., "Surface-structured diffuser by iterative down-size molding with glass sintering technology," *Opt. Express* **20**(6), 6135–6145 (2012).
16. J. Y. Kim et al., "Directly fabricated multi-scale microlens arrays on a hydrophobic flat surface by a simple ink-jet printing technique," *J. Mater. Chem.* **22**(7), 3053–3058 (2012).
17. R. Gläbe et al., "Diamond machining of micro-optical components and structures," *Proc. SPIE* **7716**, 771602 (2010).
18. L. Yu-Da et al., "New scheme of double-variable-curvature microlens for efficient coupling high-power lasers to single-mode fibers," *J. Lightwave Technol.* **29**(6), 898–904 (2011).
19. D.-H. Kim et al., "A trans-scaled nanofabrication using 3D diffuser lithography, metal molding and nano-imprinting," *J. Micromech. Microeng.* **21**(4), 045025 (2011).
20. J. Luo, Y. Guo, and X. Wang, "Rapid fabrication of curved microlens array using the 3D printing mold," *Optik* **156**, 556–563 (2018).
21. H. Ye, Z. Cao, and M. Li, "Rapid fabrication of semiellipsoid microlenses using 3D-printing and roll-to-roll imprinting process," *Microsyst. Technol.* **24**(8), 3437–3441 (2018).
22. J. Zhang et al., "Electrochemical nanoimprint lithography: when nanoimprint lithography meets metal assisted chemical etching," *Nanoscale* **9**(22), 7476–7482 (2017).
23. Z.-J. Lian et al., "Rapid fabrication of semiellipsoid microlens using thermal reflow with two different photoresists," *Microelectron. Eng.* **115**, 46–50 (2014).
24. T. Mancebo and S. Bara, "Interferometric monitoring of surface shaping processes in microlenses produced by melting photoresist," *J. Mod. Opt.* **45**(5), 1029–1037 (1998).
25. D. Hunger et al., "Laser micro-fabrication of concave, low-roughness features in silica," *AIP Adv.* **2**(1), 012119 (2012).
26. X. Meng et al., "Simple fabrication of closed-packed IR microlens arrays on silicon by femtosecond laser wet etching," *Appl. Phys. A* **121**(1), 157–162 (2015).
27. A. Pan et al., "Fabrication of concave spherical microlenses on silicon by femtosecond laser irradiation and mixed acid etching," *Opt. Express* **22**(12), 15245–15250 (2014).
28. J. Zhang et al., "Electrochemical buckling microfabrication," *Chem. Sci.* **7**(1), 697–701 (2016).
29. W. Yuan et al., "Fabrication of microlens array and its application: a review," *Chin. J. Mech. Eng.* **31**(1), 16 (2018).
30. D. L. Kendall et al., "Micromirror arrays using KOH:H₂O micromachining of silicon for lens templates, geodesic lenses, and other applications," *Opt. Eng.* **33** (11), 3578 (1994).

Bo Zhang is a postgraduate in the National Key Laboratory of Science and Technology on Multispectral Information Processing, Huazhong University of Science and Technology. His current research interests are in silicon wet etching and silicon dry etching.

Taige Liu is a PhD candidate in the National Key Laboratory of Science and Technology on Multispectral Information Processing, Huazhong University of Science and Technology. His current research interests are in silicon dry etching and silicon-based metamaterials.

Zhe Wang is a postgraduate in the National Key Laboratory of Science and Technology on Multispectral Information Processing, Huazhong University of Science and Technology. His current research interest is in liquid crystal devices.

Wenhai Huang is a postgraduate in the National Key Laboratory of Science and Technology on Multispectral Information Processing, Huazhong University of Science and Technology. His current research interests are in silicon dry etching and silicon-based metamaterials.

Chai Hu is a PhD candidate in the National Key Laboratory of Science and Technology on Multispectral Information Processing, Huazhong University of Science and Technology. Her current research interests are in silicon-based metamaterials and optical antennae.

Kewei Liu is a PhD candidate in the National Key Laboratory of Science and Technology on Multispectral Information Processing, Huazhong University of Science and Technology. Her current research interests are in liquid crystal devices and spectral imaging.

Mingce Chen is a PhD candidate in the National Key Laboratory of Science and Technology on Multispectral Information Processing, Huazhong University of Science and Technology. His current research interests are in liquid crystal devices and computational imaging.

Jiashuo Shi is a PhD candidate in the National Key Laboratory of Science and Technology on Multispectral Information Processing, Huazhong University of Science and Technology. His current research interests are in optical neural networks and metamaterials.

Xinyu Zhang is a full professor at the School of Artificial Intelligence and Automation, HUST. He received his BS degree in infrared technology from Changchun University of Science and Technology (then Changchun College of Optics and Fine-mechanics), and received his MS degree and PhD in condensed state physics and physical electronics, respectively, from HUST, Wuhan, China. He is engaged in the research of multispectral and multimodal imaging detection, micro-nano-optics, multi-spectral image processing, pattern recognition, and intelligent optics.